Full-waveform joint inversion of ambient noise data and teleseismic P waves: methodology and applications to central California

Kai Wang[1,2], Yingjie Yang[1], Chengxin Jiang[3], Yi Wang[4], Ping Tong[5,6], Tianshi Liu[7], Qinya Liu[2,7]

[1]Department of Earth and Environmental Sciences, Macquarie University, Sydney, Australia
[2]Department of Physics, University of Toronto, Toronto, Canada
[3]Research School of Earth Sciences, The Australian National University, Canberra, Australia
[4]School of Earth Sciences and Engineering, Sun Yat-sen University, Guangdong, China
[5]Division of Mathematical Sciences, School of Physical and Mathematical Sciences, Nanyang Technological University, Singapore
[6]Asian School of the Environment, Nanyang Technological University, Singapore
[7]Department of Earth Sciences, University of Toronto, Toronto, Canada

Key Points:

- We present a joint inversion scheme combining ambient noise traveltime adjoint tomography with teleseismic full-waveform inversion
- We demonstrate the advantage of the joint inversion over individual inversions using both synthetics and field data in central California
- Our model provides new constraints on the geometry of the Isabella Anomaly and helps decipher its origin.

Corresponding author: Yingjie Yang, yingjie.yang@mq.edu.au

Abstract

Adjoint tomography (i.e., full-waveform inversion) has been recently applied to ambient seismic noise and teleseismic P waves separately to unveil fine-scale lithospheric structures beyond the resolving ability of traditional ray-based traveltime tomography. In this study, we propose a joint inversion scheme that alternates between frequency-dependent traveltime inversions of ambient noise surface waves and waveform inversions of teleseismic P waves to take advantage of their complementary sensitivities to the Earth's structure. We apply our method to ambient noise empirical Green's functions from 60 virtual sources, direct P and scattered waves from 11 teleseismic events recorded by a dense linear array ($\sim$ 7 km station spacing) and other regional stations (~ 40 km average station spacing) in central California. To evaluate the performance of the method, we compare tomographic results from ambient noise adjoint tomography, full-waveform inversion of teleseismic P waves, and the joint inversion of the two data sets. Both applications to practical field data sets and synthetic checkerboard tests demonstrate the advantage of the joint inversion over individual inversions as it combines the complementary sensitivities of the two independent data sets towards a more unified model. The 3D model from our joint inversion not only shows major features of velocity anomalies and discontinuities in agreement with previous studies, but also reveals small-scale heterogeneities which provide new constraints on the geometry of the Isabella Anomaly and mantle dynamic processes in central California. The proposed joint inversion scheme can be applied to other regions with similar array deployments for high-resolution lithospheric imaging.

1 Introduction

Traditional teleseismic traveltime tomography using body waves has imaged a lot of high-resolution 3D models of mantle structures (e.g., Aki et al., 1976; van der Hilst et al., 1997; Montelli et al., 2004; Hung et al., 2004; Sigloch et al., 2008; Schmandt & Humphreys, 2010). However, due to the sub-vertical nature of ray paths of arriving teleseismic waves beneath receivers, traditional teleseismic traveltime tomography has limited resolution at shallow depths (< 50 km). On the other hand, surface wave tomography based on either earthquakes or ambient noise data can illuminate crustal and uppermost mantle structures at high resolution (e.g., Ekström et al., 1997; Ritzwoller et al., 2002; Shapiro et al., 2005; Yao et al., 2006; F.-C. Lin et al., 2007; Yang et al., 2007; Zheng et al., 2008; Saygin & Kennett, 2010; Shen et al., 2013); however, it has limited sensitivities to structures at greater depths ($>\sim 250$ km). The apparent complementary sensitivities of surface waves and teleseismic body waves to the Earth's subsurface structures have motivated the development of inversion schemes that jointly invert the two data sets. Various applications based on surface wave dispersions and body wave traveltimes have been developed, and have demonstrated the feasibility of joint inversions for constructing a more unified model than separate inversions across different scales (e.g., Woodhouse & Dziewonski, 1984; Friederich, 2003; West et al., 2004; Obrebski et al., 2011; H. Zhang et al., 2014; Nunn et al., 2014; Fang et al., 2016; Guo et al., 2018; Jiang, Schmandt, Ward, et al., 2018). Nevertheless, such a traveltime-based joint inversion scheme has several limitations: (1) it is formulated based on ray theory or other approximation of wave propagation theories where structural sensitivity kernels are calculated without considering 3D lateral heterogeneities; (2) model parameters are usually velocity perturbations relative to a 1D reference model rather than absolute values as teleseismic differential traveltimes are often used in the inversion; (3) traveltimes of primary phases (such as direct P and S waves) are most sensitive to long-wavelength structures (e.g., Liu & Gu, 2012), thus offering limited resolution.

Compared with the traditional traveltime tomography, *full-waveform inversion* (FWI, also known as *adjoint tomography* in earthquake seismology) based on 3D numerical modeling of seismic wave propagations can account for more realistic 3D sensitivity kernels, and thus it can resolve sub-wavelength structural heterogeneities (Virieux & Operto, 2009; Liu & Gu, 2012; Tromp, 2020). Over the past decade, an increasing number of applications based on FWI techniques have been conducted in various regions using earthquake data (e.g., C. Tape et al., 2009; Fichtner et al., 2009; Zhu et al., 2012; Chen et al., 2015; Bozdağ et al., 2016; Krischer et al., 2018; Tao et al., 2018; Lloyd et al., 2020), unveiling unprecedented details of the Earth's interior beyond the resolvability of traditional ray-based tomography. More recently, FWI has been further extended to applications using teleseismic body waves (e.g., Y. Wang et al., 2016; Beller, Monteiller, Operto, et al., 2018) and empirical Green's functions from ambient seismic noise data (e.g., Gao & Shen, 2014; Chen et al., 2014; C. Zhang et al., 2018; K. Wang et al., 2018, 2020; Lu et al., 2020; Sager et al., 2020).

Teleseismic full-waveform inversion (TeleFWI) of high frequency P waves (including direct and scattered waves) has been demonstrated to be capable of resolving small-scale structures beneath dense linear arrays through the implementation of hybrid methods (Tong, Chen, et al., 2014; Tong, Komatitsch, et al., 2014; Monteiller et al., 2013, 2015; Masson & Romanowicz, 2016; C. Lin et al., 2019; Pienkowska et al., 2020). The hybrid methods couple a regional 3D numerical solver for a small target area with an external fast numerical/analytical method for a 1D background model. Utilizing the waveform information of scattered waves on both vertical and radial components, TeleFWI not only resolves small-scale local heterogeneities and sharp velocity discontinuities but also allows constraints on multiple model parameters, such as density, Vp and Vs. However, this method usually relies on the coherence of the scattered wavefields across stations which requires dense seismic arrays with small station spacing. For example, previous studies (Y. Wang et al., 2016; Beller, Monteiller, Operto, et al., 2018) have shown that TeleFWI based on 5-50 s P and coda waves recorded by a dense linear seismic array with ~ 8 km inter-station spacing, can resolve structural anomalies with a lateral dimension of ~ 20 km (close to the minimum wavelength). Although this technique can image high-resolution structures using data from dense seismic arrays, it suffers from increasing spatial aliasing effects when the station spacing becomes larger. In reality, dense seismic arrays with a station spacing of 10 km or less are usually deployed as linear arrays for receiver function analysis or migration studies only in selected regions around the globe. Most seismic arrays for tomographic studies are designed to be nearly evenly distributed over a region with a much coarser station spacing (≥ 30 km), such as the USArray Transportable Array and ChinArray. Nevertheless, Beller, Monteiller, Combe, et al. (2018) demonstrate that additional stations from other coarser seismic networks can help improve the lateral resolution and penetration depth of TeleFWI compared with only using a 2D dense linear array.

Different from TeleFWI, the lateral resolution of ambient noise tomography mostly depends on station distribution as it relies on surface waves extracted from cross-correlations between station pairs. Benefiting from accurate 3D structural sensitivity kernels, ambient noise adjoint tomography (ANAT) or full-wave ambient noise inversion has demonstrated its potential in resolving more pronounced velocity variations than ray-theory based ambient noise tomography (e.g., Gao & Shen, 2014; Chen et al., 2014; K. Wang et al., 2018; Sager et al., 2020; Lu et al., 2020). To date, most ANAT studies only use traveltime misfits to obtain the optimal Vs model as amplitude information is usually not well retained during most ambient noise data preprocessing procedures (Bensen et al., 2007). Since ANAT and TeleFWI have complementary constraints on resolving Vs structures, the two methods can be combined into the same framework of adjoint tomography. C. Zhang et al. (2020) investigated such a concept of joint inversion of ambient noise and teleseismic body waves based on 2D adjoint tomography. To our best knowledge, a joint inversion of ambient noise and teleseismic body waves in the framework of 3D adjoint tomography has not been implemented and applied to either synthetics or real data sets. Such joint inversions can take advantage of both an accurate 3D numerical solver and the iterative inversion scheme, and thus are expected to reduce the aforementioned limitations in traditional traveltime tomography. In addition, TeleFWI also provides additional constraints on Vp and density structures which may help further improve the Vs image of ANAT.

Inspired by the success of joint surface-wave and teleseismic body-wave inversions in traditional traveltime tomography (e.g., Obrebski et al., 2011; H. Zhang et al., 2014; Nunn et al., 2014; Guo et al., 2018), in this study we develop a joint inversion scheme combining the complementary sensitivities of ANAT and TeleFWI. We apply the method to both synthetic and field data sets in central California (Figure 1a). We first demonstrate the advantages of the joint inversion by comparing the resulting velocity models with those from separate inversions (ANAT and TeleFWI) in practical field data applications and 3D synthetic checkerboard tests. Then, the final model from the joint inversion is compared with velocity models from traditional traveltime tomography and also with structural interfaces mapped from receiver function analysis. In the end, we will discuss both the advantages and limitations of our joint inversion in resolving small-scale lithospheric structures.

2 Methodology

2.1 Traveltime and waveform inversions

For traveltime adjoint tomography of ambient noise (i.e., ANAT), we seek to minimize the traveltime misfits between empirical Green's functions (EGFs) from noise cross-correlations and synthetic Green's functions (SGFs) from point-force sources (K. Wang et al., 2019). In this study, we measure the frequency-dependent traveltime misfits expressed as:

$$\phi^T = \frac{1}{2}\sum_{i=1}^{N}\int_{-\infty}^{+\infty}\frac{h_i(\omega)}{H_i}\left[\frac{\Delta T_i(\omega,\mathbf{m})}{\sigma_i}\right]^2 d\omega\,, \tag{1}$$

where $\mathbf{m}$ denotes the model vector, $\Delta T_i(\omega,\mathbf{m})$ represents the frequency-dependent traveltime difference between the ith pair of SGF and EGF with its uncertainty σ_i, $h_i(\omega)$ is a frequency-domain window normalized by $H_i = \displaystyle\int_{-\infty}^{+\infty} h_i(\omega)\,d\omega$, and N is the number of measurements. The detailed expression of adjoint source for multitaper traveltime measurements are listed in Appendix C of C. H. Tape (2009).

Time-domain FWI seeks to minimize the least-square waveform misfit function (ϕ) between N number of observed data and the corresponding synthetics expressed as:

$$\phi = \sum_{i=1}^{N}\int_{t1}^{t2}\frac{1}{2}\|\mathbf{u}_i(t)-\mathbf{d}_i(t)\|^2\mathrm{d}t, \tag{2}$$

where $\mathbf{d}_i(t)$ and $\mathbf{u}_i(t)$ denote the three-component waveforms of data and synthetic for the ith window between $[t1,t2]$. Due to the well-known source-structure tradeoff, accurate source wavelet estimation plays an important role in a successful FWI (Pratt, 1999; Virieux & Operto, 2009) and the effects of source-side surface-reflected multiples can be taken into account by convolving synthetics $\mathbf{u}_i(t)$ with an estimated source wavelet $W(t)$ (Bostock, 2004). Thus, a new waveform misfit function (ϕ^W) between data and the convolved synthetics is adopted in practice

$$\phi^W = \sum_{i=1}^{N} \int_{t1}^{t2} \frac{1}{2} \|\mathbf{u}_i(t) * W(t) - \mathbf{d}_i(t)\|^2 \mathrm{d}t. \tag{3}$$

where the symbol $*$ represents the convolution operator. As demonstrated by Plessix (2006) and Beller, Monteiller, Operto, et al. (2018), the adjoint source of this new waveform misfit function is

$$f_i^{W\dagger}(t) = W(t) \star [\mathbf{u}_i(t) * W(t) - \mathbf{d}_i(t)], \tag{4}$$

where the symbol $\star$ represents the correlation operator.

The adjoint sources are placed at receivers to generate the adjoint wavefield which interacts with the forward wavefield to generate sensitivity kernels defined in the linear relationship between the perturbations of misfit function ($\delta\phi$) and model variations

$$\delta\phi = \oint \left[K_\rho(m)\delta\ln\rho + K_\alpha(m)\delta\ln\alpha + K_\beta(m)\delta\ln\beta\right] dV, \tag{5}$$

where $K_\rho(m), K_\alpha(m), K_\beta(m)$ are the sensitivity kernels for density (ρ), Vp (α) and Vs (β) (Tromp et al., 2005; Liu & Tromp, 2006; K. Wang et al., 2019).

2.2 Joint inversion algorithm

We adopt a joint inversion algorithm originally developed for exploration seismic data by Sun et al. (2017), and reformulate it for deep Earth imaging based on the adjoint tomography of ambient noise and teleseismic data. The iterations of this method alternate between traveltime and waveform inversions which has the advantage of avoiding nonphysical scaling factors between different data sets used in conventional joint inversions (e.g., Obrebski et al., 2011; H. Zhang et al., 2014). It is implemented through the following four steps:

1. At the beginning of the first iteration ($k = 0$), the initial model is set to be either a 1D reference model or a 3D model from previous seismic imaging studies.
2. Apply ANAT to minimize the traveltime misfits (eq. 1) of Rayleigh waves between EGFs and SGFs, and obtain a new model $\mathbf{m}_{tt}$.

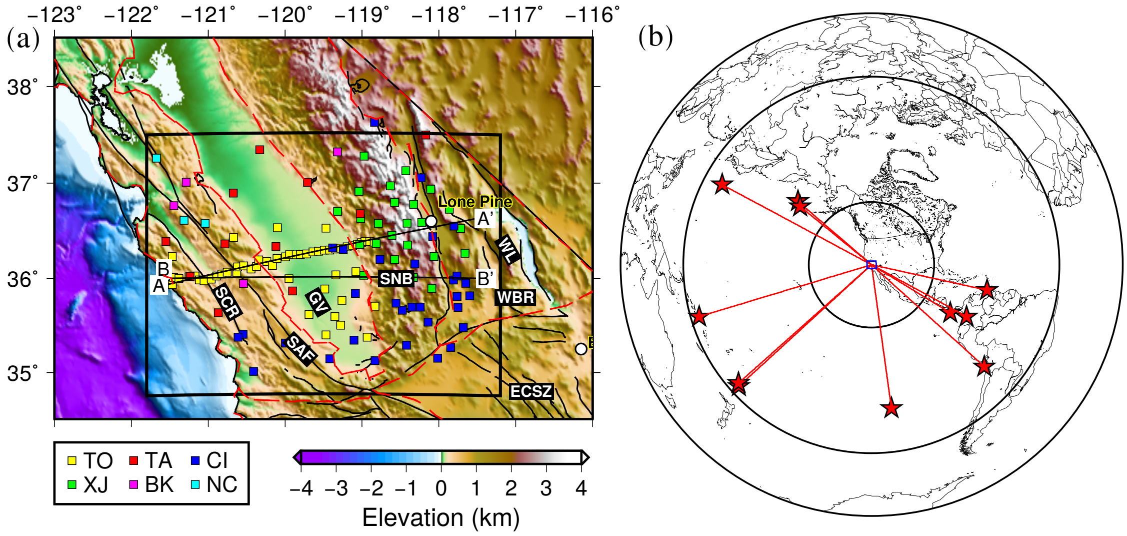

Figure 1. (a) Map of topography and station distribution in the study area. Stations from six seismic networks are plotted by rectangles filled with different colors as specified in the left bottom box. The black lines denote the locations of the two cross-sections that we will present our models in the following. The thick black box represents the simulation domain. Geologic abbreviations: SCR, Southern Coast Ranges; GV, Great Valley; SAF, San Andreas Fault; SNB, Sierra Nevada Batholith; WL, Walk Lane; WBR, Western Basin Ranges; ECSZ, Eastern California Shear Zone. (b) Location of the 11 teleseismic events (red stars) used in teleseismic full-waveform inversion. The two circles inside denote the boundaries of epicentre distances at 30° and 90°, and the blue rectangle is the study region.

3. Update the model as $\mathbf{m}_{k+1} = \mathbf{m}_{tt}$. If the total misfit reduction over ANAT is less than a small value, such as 3% we choose in this study, iteration terminates; otherwise, set $k = k + 1$, and continue to the next step.
4. Apply TeleFWI to minimize the teleseismic P waveform differences (Eq. 3) between observations and synthetics computed based on hybrid methods, and obtain a new model $\mathbf{m}_{wf}$.
5. Update the model by $\mathbf{m}_{k+1} = \mathbf{m}_{wf}$. If the total misfit reduction over TeleFWI is less than 3%, iteration terminates; otherwise, set $k = k + 1$, and go back to step 2.

3 Application to seismic data in central California

We apply this joint inversion method to image the lithospheric structure beneath central California to examine its feasibility and robustness. Our data sets consist of surface waves extracted from ambient noise cross-correlations and teleseismic P waveforms (including the direct P and its coda) recorded by 128 stations in central California (Figure 1a). These stations come from six seismic networks, including TO from the Central California Seismic Experiment (CCSE) deployed between 2013-2015, XJ from the Sierran Paradox Experiment in 1997, regional permanent networks (NC, CI and BK) and the USArray Transportable Array (TA). In particular, the dense CCSE array ($\sim$ 7 km station interval) provides a high spatial sampling of teleseismic P scattered waves that are essential for resolving small-scale structures beneath the array. Other off-line stations sparsely distributed with an average of ~ 40 km inter-station distance help capture scattered waves in all directions more completely, and thus can improve the lateral resolution (Beller, Monteiller, Operto, et al., 2018).

3.1 Data processing

We obtain ambient noise cross-correlation functions (CCFs) between station pairs from the TO and CI networks using the python package of NoisePy (Jiang & Denolle, 2020), in which the standard noise processing procedure of Bensen et al. (2007) is followed. We also add CCFs of station pairs that are located within our study area and have been previously extracted by Xie et al. (2018) from other networks. These CCFs are filtered at the period band of 5-50 s and only those with an average signal-to-noise ratio (as defined in Bensen et al., 2007) larger than 5 are retained for tomography. In the end, 60 virtual sources are selected for the later inversion, resulting in 3167 ray paths that fairly uniformly cover our study region (Figure S1). CCFs are converted to EGFs by a reversed time derivative as similarly done in K. Wang et al. (2018). In this study, we only use the Rayleigh waves from vertical-vertical component EGFs for adjoint tomography.

To obtain reliable scattered waves from teleseismic events, we apply a series of selection criteria for data quality control similar to those in Beller, Monteiller, Operto, et al. (2018). First, we select 345 teleseismic events with (1) magnitudes $>= 5.8$, (2) epicentral distances to the center of the study region within $30° - 90°$, and (3) hypocentral depths in the range of 0-30 km or 180-1000 km. The last event selection criterion on hypocentral depth is to ensure that teleseismic waveforms are less contaminated from source-side surface reflections, such as pP. For each event, we collect three-component waveforms within time windows defined as two minutes before and three minutes after the direct P arrivals predicted by the AK135 model (Kennett et al., 1995). We then remove the instrument response, mean values, linear trends from the five-min time series, and rotate north and east components to radial and transverse components. Afterwards, the pre-processed three-component waveforms of each event

Table 1. Event information and parameters of plane wave injection, including event origin time, longitude (Lon), latitude (Lat), depth, back-azimuth (Baz) and incident angle (Inc_ang) to the center of the array.

Event ID	Origin time	Lon (°)	Lat (°)	Depth (km)	Baz (°)	Inc_ang (°)
5	2014/04/01 23:46:47	-70.7691	-19.6097	25.0	131.460	18.09
12	2014/06/23 19:19:15	-177.7247	-29.9772	20.	227.414	15.09
13	2014/06/24 03:15:35	176.6981	52.2045	4.	310.964	24.08
27	2014/10/09 02:14:31	-110.8112	-32.1082	16.54	171.613	19.02
29	2014/12/08 08:54:52	-82.6865	7.9401	20.	120.220	24.69
37	2015/05/30 11:23:02	140.4931	27.8386	664.	297.892	15.32
42	2015/08/15 07:47:06	163.8226	-10.8968	8.	253.108	15.03
45	1997/07/09 19:24:13	-63.4860	10.5980	19.9	102.334	21.73
46	1997/09/02 12:13:22	-75.7499	3.8490	198.7	118.403	22.65
51	1997/09/20 16:11:32	-177.6240	-28.6830	30.0	228.525	15.16
58	1997/06/17 21:03:04	-179.3320	51.3470	33.0	309.119	24.60

are visually inspected; and only those with (4) high signal-to-noise ratios and (5) spatial coherent signals on both vertical and radial components across the array are retained. For each vertical and radial component of an event, we then use the open-source software AIMBAT (Lou et al., 2013) to align the waveforms as well as to obtain the array stacked trace, and remove traces with (6) cross-correlation coefficients less than 0.90. In total, we select 11 teleseismic events (Figure 1b) that satisfy the above data selection criteria for the following inversion. The detailed information of these 11 events is listed in Table 1.

3.2 Inversion procedures

We perform all the forward and adjoint simulations based on the open-source spectral-element method (SEM) package, SPECFEM3D (Komatitsch & Vilotte, 1998; Peter et al., 2011) and the adjoint-state technique (Liu & Tromp, 2006). The simulation domain (Figure 1a) extends from 121.8°W to 117.2°W ($\sim$ 400 km), from 34.75°N to 37.5°N ($\sim$ 320 km), and from the surface to 220 km in depth. Its mesh has 80 and 60 elements in longitudinal and latitudinal directions respectively, and 25 layers in depth. The mesh is irregular with an element size of 5 km at the top (0-30 km) and 10 km at the bottom (30-220 km), giving a minimum resolving period of 3.5 s and a maximum time step of 0.03 s. In our inversion, we choose a time step of 0.025 s, a 120 s duration to simulate teleseismic P waves and a 170 s duration for surface waves.

Following the algorithm outlined in section 2.2, the joint inversion starts from a smoothed AK135 model (Kennett et al., 1995) (Figure S2) and proceeds by alternating ANAT and Tele-FWI inversions to update the density and velocity structures. For ANAT, we follow similar inversion procedures as described in K. Wang et al. (2018). We first place vertical point-force sources with a Gaussian source time function of 1.0 s half duration at the surface to generate vertical-component SGFs at receivers. Then, EGFs and SGFs are filtered at three narrow period bands: namely 6-15 s, 10-20 s and 15-35 s. A multi-taper technique (e.g., Zhou et al., 2004; C. Tape et al., 2009) is adopted to measure the frequency-dependent traveltime difference (Eq. 1) between each EGF-SGF pair within the surface-wave time window determined by its phase velocity dispersion. The corresponding adjoint sources are calculated accordingly.

For forward simulations in TeleFWI, we adopt a hybrid method, FK-SEM, to compute the response in the simulation domain to the teleseismic wavefield from a plane wave injection. The FK-SEM method interfaces the numerically efficient frequency-wavenumber (FK) calculations for a 1D background model outside the domain with the accurate spectral-element computations for 3D models within the domain (Tong, Chen, et al., 2014; Tong, Komatitsch, et al., 2014). The initial wavefronts of the injected plane waves start from a reference point beneath the center of the array where incident angles and back-azimuths are also calculated for the various events as listed in Table 1. The depth of the reference point is defined at 400 km so as to ensure the initial wavefronts of the 11 teleseismic events do not enter the boundaries of the local simulation domain. The predicted arrival times of direct P waves from a plane wave are given by the traveltime delays between the initial wavefront and receivers computed for the AK135 model (see Appendix A for details). In order to compare data with the synthetics, waveforms of observed teleseismic P waves are first aligned by subtracting the reference direct P arrivals predicted from the AK135 model, and then shifted by the predicted first arrivals from the initial wavefronts to receivers. We then apply a time domain deconvolution method (e.g., Kikuchi & Kanamori, 1982; Lay et al., 2009) in conjunction with principal component analysis (PCA) (e.g., Halldor & Venegas, 1997) to obtain the source wavelet signature from vertical components (Y. Wang et al., 2016; Beller, Monteiller, Operto, et al., 2018). Figure 2 shows an example of the general processing procedures similar to those used by Y. Wang et al. (2016), as summarized in the following four steps:

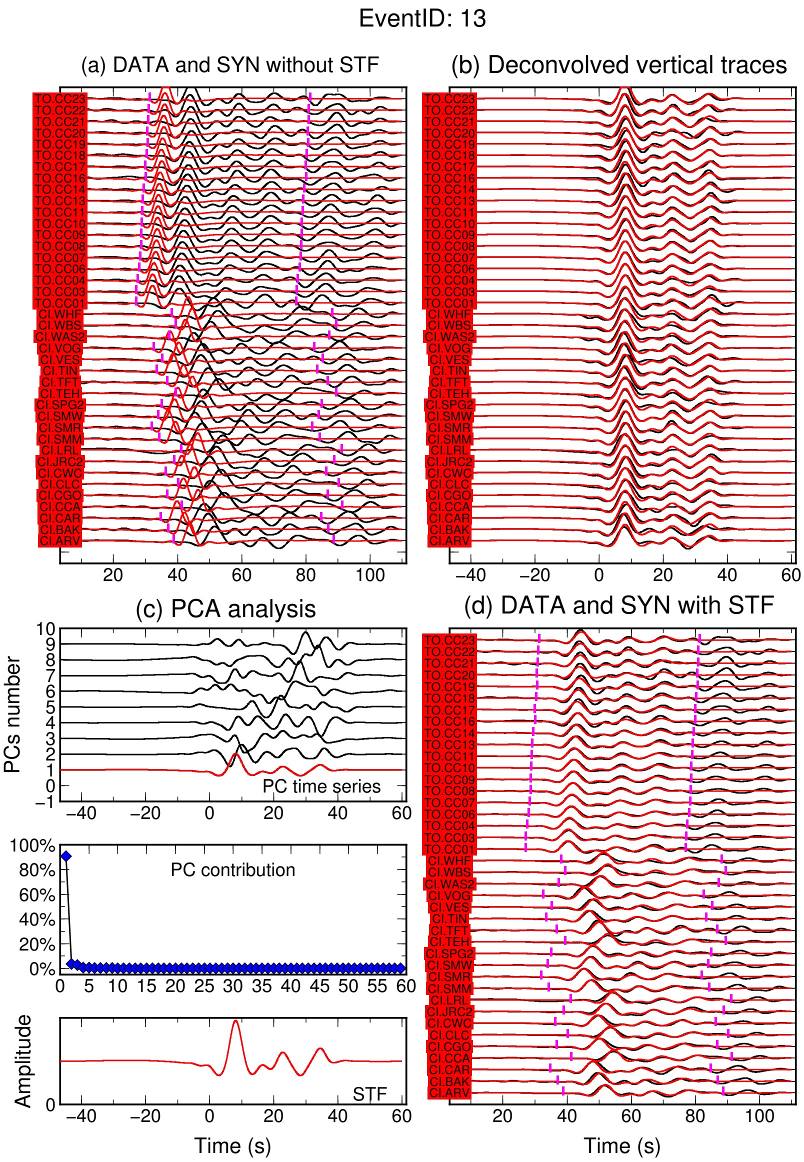

Figure 2. An example of the four processing steps to obtain the average source wavelet signature (i.e., STF, source time function) and waveform differences for event 13. (a) Data (black) and synthetics (red) filtered at the period band of 5-50 s. (b) Candidate STFs (black) obtained by deconvolving the synthetic from the data based on the time domain deconvolution method. The waveforms in red color denote the primary principal component (PC) of the STFs in c. (c) Top: Time series of the first nine PCs; Middle: Contribution of each PC; Bottom: the primary PC used as the average STF. (d) Data (black) and new synthetics (red) convolving with the average STF. Purple bars in (a) and (d) represent the time windows ([-5, 45] s relative to direct P arrivals) for measuring the waveform differences.

1. Data and synthetic waveforms are first filtered between 5-50 s. Observed data are also normalized by the maximum of the record section (Figure 2a) to balance the displacement amplitudes from earthquakes of different magnitudes in the inversion.
2. Based on the time-domain iterative deconvolution method (e.g., Kikuchi & Kanamori, 1982; Lay et al., 2009), the synthetics on the vertical component are deconvolved from their corresponding data to obtain the candidate source wavelets (Figure 2b).
3. PCA is applied to these candidate source wavelets to obtain different data modes (i.e., principal components) and the first mode which accounts for at least 80% contribution is regarded as the average source wavelet signature (Figure 2c).
4. The synthetics on both vertical and radial components are convolved with this average source wavelet and then compare with corresponding shifted observed data to calculate waveform differences and adjoint sources (Figure 2d).

For each teleseismic event or virtual source, we calculate the event kernel by injecting the adjoint sources at receivers based on the adjoint-state method (Liu & Tromp, 2006). Then, all event kernels are summed, preconditioned and smoothed to obtain the final misfit gradient for model updating. A preconditioner given by the square root of depth (Y. Wang et al., 2016) is used to approximate the Hessian matrix to accelerate the convergence of the inversion. In the first several iterations, the horizontal and vertical radii of the 3D Gaussian function used to smooth the gradient are 20 km and 10 km, respectively. Then, they are reduced to smaller values of 10 km and 5 km to resolve smaller scale structures in later iterations. During the inversion, the optimization is achieved through the L-BFGS algorithm (Chap 9, Nocedal & Wright, 2006) and a line search method is used to determine the optimal step length for model updating.

To demonstrate the advantage of our joint inversion framework, we also conduct two additional separate inversions either only using ambient noise data or only using teleseismic data. The separate inversions also begin with the smoothed AK135 model and use the same inversion parameters as the joint inversion including the smoothing radii and step lengths. In total, we conduct three inversions: (1) traveltime adjoint tomography of ambient noise surface waves (i.e., ANAT); (2) waveform inversion of teleseismic P and scattered waves (i.e., Tele-FWI); (3) joint inversion alternating between the two data sets (i.e., Joint).

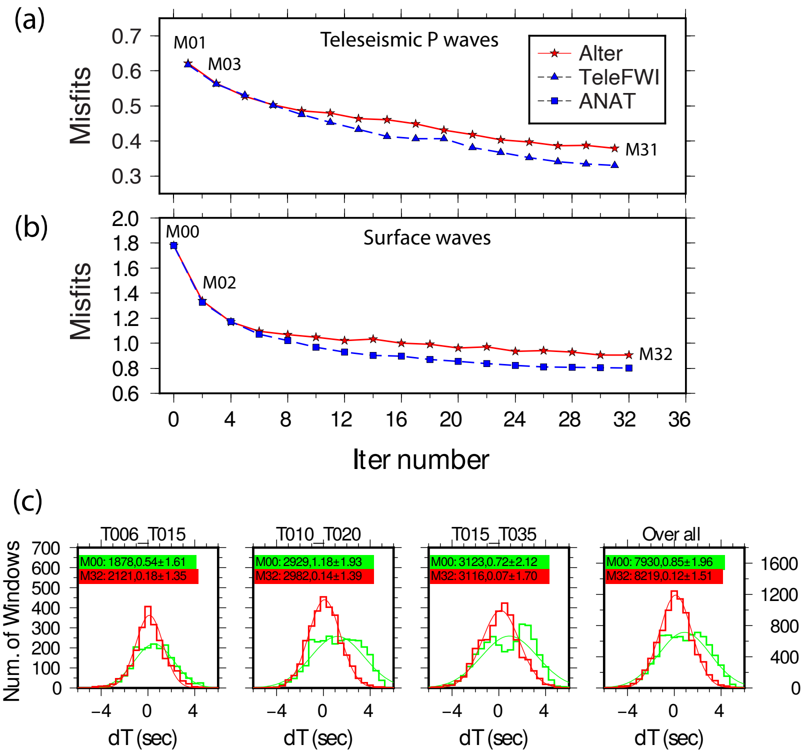

Figure 3. The total misfit evolution for (a) teleseismic P waveforms and (b) ambient noise surface waves over iterations in ANAT (blue rectangles), TeleFWI (blue triangles) and the joint inversion (red stars). The joint inversion starts from the smoothed AK135 model (M00), and alternatively fits surface wave (M00, M02, $\cdots$, etc) and body wave (M01, M03, $\cdots$, etc) data sets. Iteration numbers of ANAT and TeleFWI are multiplied by 2 to match those of the joint inversion. (c) Differential traveltime histograms between EGFs and SGFs for the initial (green) and final (red) models at three periods bands, i.e., 6-15 s, 10-20 s, 15-35 s for the joint inversion. The histograms of overall misfits are shown in the last column.

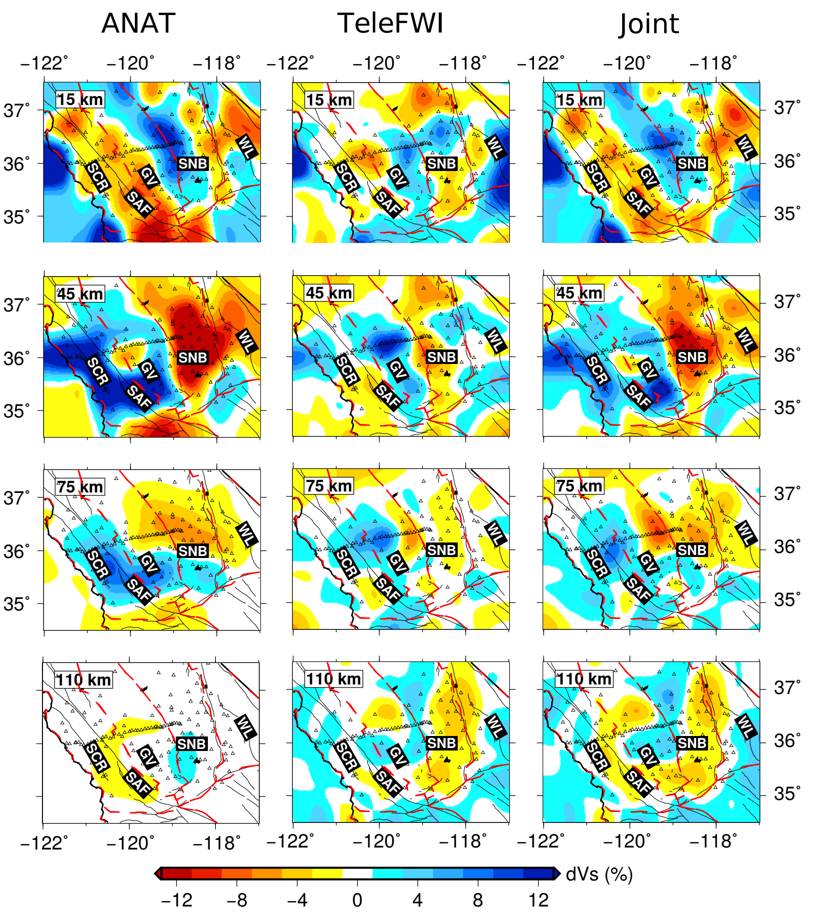

301 **Figure 4.** Horizontal slices of Vs images from ANAT (left columns), TeleFWI (middle columns) and the
302 joint inversion (right columns) at depths of 15 km, 45 km, 75 km and 110 km.

3.3 Joint inversion results

Figure 3a and 3b present the total misfit evolution of teleseismic P waveforms and ambient noise surface wave traveltimes respectively for the two separate inversions and the joint inversion. In general, the joint inversion shows a slower convergence rate and slightly larger misfits than those from separate inversions. A similar pattern has also been seen in the traveltime joint inversion by Fang et al. (2016) which is reasonable as the joint inversion scheme tries to fit both data sets simultaneously. The joint inversion converges after 32 iterations when the misfit changes over the last iteration for both noise and teleseismic data are less than 3%. The final misfit reductions of the teleseismic (from 0.62 to 0.37) and ambient noise (from 1.77 to 0.90) data are about 40.3% and 49.2% respectively. Figure 3c shows the differential traveltime histograms between EGFs and SGFs for the initial and final model from the joint inversion. It is clear that this final model improves the data fitting significantly in comparison with the initial model, with a smaller overall average misfit and standard deviation (e.g., $0.85\pm$ 1.96 s to 0.12 ± 1.51 s).

To compare the results from the three types of inversions, we show their final Vs models at 15, 45, 75 and 110 km depths respectively in Figure 4. In general, the Vs images from ANAT agree well with the first-order velocity structures from previous tomographic studies (Yang et al., 2008; Moschetti et al., 2010; Shen et al., 2013; Jones et al., 2014; Jiang, Schmandt, Hansen, et al., 2018; Bernardino et al., 2019). For example, high velocities ($+10\%$) referred to as the Foothills Anomaly (FA), are observed in the crust along the western foothills of Sierra Nevada Batholith (SNB), as also seen in the teleseismic P-wave tomography of Jones et al. (2014). Surrounding the FA, relatively low velocities are observed in the Great Valley (GV) (-3%), the eastern SNB and Walker Lane (WL) region (-6%). In the uppermost mantle (45 km), the whole SNB and WL region exhibit strong low velocities (-12%) while the western coast shows relatively high velocities. At this depth, ANAT also reveals a low velocity zone under the central GV that is not seen in previous surface wave tomography (Shen et al., 2013; Jiang, Schmandt, Hansen, et al., 2018). This anomaly might be influenced by the shallow thick sediments (< 10 km) in GV which cannot be well constrained by ANAT due to the lack of short-period dispersion information. A similar fast-to-slow velocity feature from the coast to the northeast further extends to the depth of 75 km with smaller amplitudes, and almost no change of the Vs is obtained at greater depths (i.e., 110 km) due to degrading depth sensitivities of surface waves. Compared to ANAT, TeleFWI resolves similar Vs patterns in the crust but with smaller amplitudes. The major difference between the two models exists in the up-

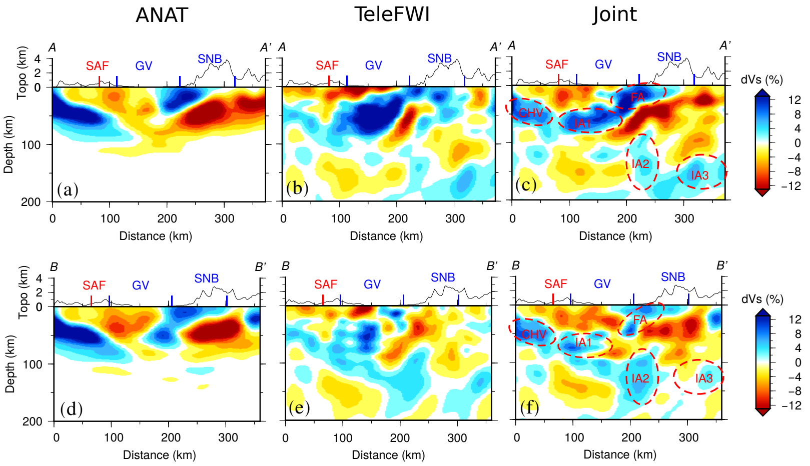

Figure 5. Vertical cross-sections (a-c) AA' and (d-f) BB' of Vs images from the ANAT (a, d), TeleFWI (b, e) and joint (c, f) inversions. High Vs zones: CHV-Coastal High Velocities; IA-Isabella Anomaly; FA-Foothills Anomaly.

permost mantle where TeleFWI reveals a dominating high velocity body centered at 119.5°W and 36°N known as the Isabella Anomaly (IA) (e.g., Raikes, 1980; Jones et al., 1994). Moreover, TeleFWI reveals deeper Vs structures (e.g., 110 km) which are below the penetration depth of ANAT. The final Vs model from the joint inversion accommodates the features from both ANAT and TeleFWI, including the three high velocity zones (FA, IA and coastal high velocities) and the low velocity zone beneath the eastern SNB and WL.

In addition, we also show two vertical cross-sections (locations indicated in Figure 1a) of Vs structures to further examine the depth extent of the aforementioned velocity anomalies, particularly the FA and IA. The AA' profile (Figure 5a-c) follows the dense linear array and extends eastward into the eastern SNB. In the ANAT model, the coastal high velocity body is observed to dip sub-horizontally eastward with an overriding wedge-like low velocity zone beneath the central GV. Under the western SNB, the high velocity FA ($+10\%$) is mostly confined to the upper 50 km, while low velocities (-12%) show up at greater depths that extend upward to the east towards the eastern SNB (Figure 5a). In comparison, TeleFWI only reveals a weak (-4%) east-dipping coastal high velocity body and the strong low velocities (-12%) beneath GV is mostly confined to the shallow crust. The high velocity features identified in the upper mantle as IA1 seems to be connected to the shallow FA, in company with a strip-like low velocity body below (Figure 5b). The model from the joint inversion (Figure 5c) shows the three high Vs bodies (coastal high velocities, IA1 and FA) are connected and also shows the low velocities beneath the SNB are merged to form an oblique low velocity zone from the eastern SNB to below IA1. At greater depths, two high Vs bodies (IA2 and IA3) are imaged beneath the SNB and may be interpreted as the deeper parts of the IA (Bernardino et al., 2019; Y. Wang et al., 2013).

Another profile (BB') along the latitude 36°N is shown to facilitate model comparisons with previous tomography models (Jiang, Schmandt, Hansen, et al., 2018; Yang et al., 2008; Jones et al., 2014; Bernardino et al., 2019). In general, the velocity variations along this profile is similar to those along AA' in the top 80 km. The amplitudes of the velocity anomalies from TeleFWI decrease from the profile AA' to BB', probably due to coarser station intervals off-line of the dense CCSE array. The major feature seen in BB' that differs from AA' is that the IA1 is connected with the deeper IA2 instead of the shallow FA.

4 Discussions

4.1 Synthetic tests and model resolution

We conduct several numerical experiments to further demonstrate the advantage of the joint inversion over separate inversions and to assess the model resolution. Synthetic data is computed for checkerboard models with $\pm 12\%$ perturbations relative to the smoothed AK135 background model, and simulated with the same source time functions as those used in the practical inversions. Then, we conduct the joint inversion and two separate inversions following the same inversion procedures described in section 3.2. Figure 6 displays the recovered checkerboard models with anomaly sizes of ~ 40 km from ANAT, TeleFWI and the joint inversion, respectively. It is clear that surface waves from this study are mostly sensitive to Vs structures at shallow depths (< 60 km) which is limited by the frequency range of retrieved cross-correlations from ambient noise. Compared with ANAT, TeleFWI is sensitive to much deeper structures for all three model parameters (ρ, V_p and V_s). However, it suffers from strong smearing shown in the horizontal cross-sections of the recovered models (Figure 6, middle columns) due to the near-vertical incidence of teleseismic P waves beneath the sparsely distributed receivers. Benefiting from the more uniform ray-path coverage between station pairs, surface waves help better illuminate structures at the off-line areas that are not well resolved in TeleFWI. Thus, the addition of surface waves in the joint inversion helps alleviate the strong smearing at shallow depths. At greater depths, the joint inversion shares a similar resolution of the TeleFWI with slightly degraded amplitude recovery. These tests demonstrate that the joint in-

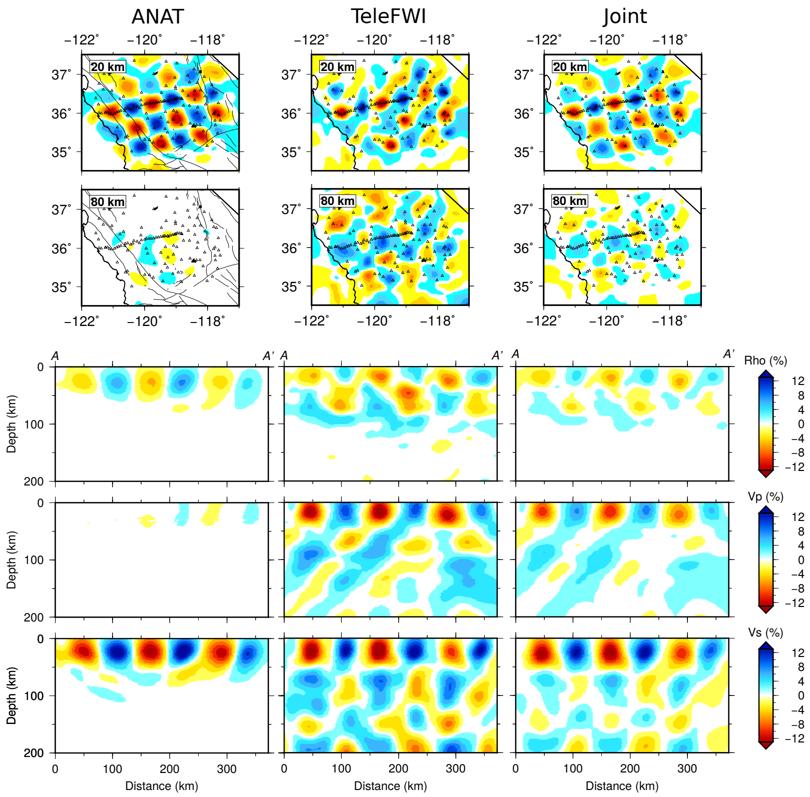

Figure 6. Recovered models of 40 km size 3D checkerboard tests for ANAT (left columns), TeleFWI (middle columns) and the joint inversion (right columns). The top two rows exhibit the Vs models at depths of 20 km and 80 km, respectively. The last three rows show the models of density, Vp and Vs beneath the AA' profile.

version combining the complementary sensitivities of surface waves and teleseismic P waves is capable of building a more unified model, thus outperforming inversions based on individual data sets.

We further evaluate the model resolution based on synthetic tests using the TeleFWI scheme instead of the joint inversion. Since joint inversions are too computationally extensive for a series of synthetic models as shown latter, we use TeleFWI checkerboard test as a good approximation to the model resolution for the joint inversion, except at shallow depths where additional checkerboard tests with a 40 km anomaly size have already been performed (Figure 6). The synthetic models are composed of a series of 3D checkerboard anomalies with sizes of 20 km, 40 km and 80 km. In particular, two sets of anomaly distributions are designed to specifically investigate the resolution along profiles AA' (Figures S3-S4) and BB' (Figures S5-S6), respectively. The results from these synthetic tests suggest that the resolution beneath the

CCSE array for the Vs model decreases from 20 km at the top to 40 km at the bottom. As P waves have longer wavelengths than S waves, the Vp structure is less resolved in comparison with the Vs structure and the resolution is about 40 km in the upper 100 km and 80 km at greater depths. The resolution of the density is degraded from that of the Vs, and it can be only resolved in the upper 60 km. The resolutions of the three model parameters for the BB' profile are similar to those for the AA' profile. However, profile AA' shows slightly stronger smearing effects at depths below 50 km likely due to the existence of fewer stations north of the profile compared to those for BB'. Since the density and Vp models have limited resolution, we mainly focus our discussion on the Vs structures in this study.

4.2 Model comparison and implications

Central California is located in a tectonically complex region where the lithospheric structures are shaped by a prolonged tectonic history involving slab subduction, plate boundary transformation and associated mantle dynamics. Previous tomographic studies (e.g., Jones et al., 1994; Zandt et al., 2004; Boyd et al., 2004; Yang et al., 2008; Jones et al., 2014; Jiang, Schmandt, Hansen, et al., 2018; Bernardino et al., 2019) have provided valuable information on the seismic structures of this region. However, the resolution scale of previous tomographic studies in the upper mantle is limited to about 60 km or larger. In this section, we compare the velocity models of central California from our joint inversion with those from traditional ray-theory based methods to demonstrate the feasibility and advantage of our method in practical tomography. In particular, we focus on some interesting small-scale features revealed in our model that are beyond the resolution of traditional methods, and discuss their associated tectonic implications.

Figure 7 shows the comparison of seismic features seen in our final Vs model with (1) the interfaces inferred from common conversion-point (CCP) image of Sp receiver functions by Hoots (2016) and (2) the Vs model from surface wave tomography based on ambient noise and teleseismic surface wave data by Jiang, Schmandt, Hansen, et al. (2018), hereafter called `Jiang2018` model. Our new Vs model shows drastically better coincidence with interface structures revealed by the receiver function study of Hoots (2016) compared to the `Jiang2018` model due to the consideration of scattered wave energy within TeleFWI, clearly illustrated at two regions with receiver function results. First, at the west end of the two cross-sections, a prominent high velocity anomaly is observed in the lithosphere and dips to the east reaching $\sim$ 100 km depth beneath the SAF. This feature exhibits a similar pattern in profiles AA'

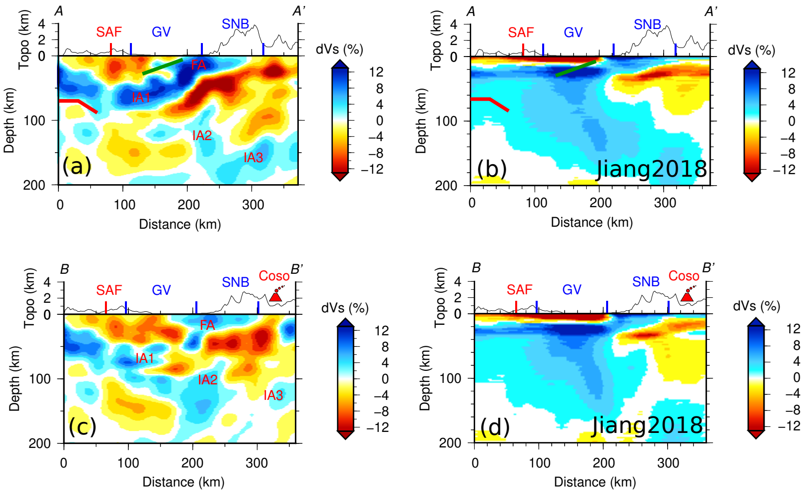

Figure 7. Comparison of Vs images along profiles (a-b) AA' and (c-d) BB' from this study and the one from Rayleigh wave tomography (Jiang2018) by Jiang, Schmandt, Hansen, et al. (2018). The thick green and red lines in (a) and (b) denote the velocity contrasts from Sp receiver function (Hoots, 2016).

and BB' and its bottom depth is consistent with the lithosphere–asthenosphere boundary (LAB) identified by the Sp receiver function analysis of Hoots (2016). This boundary has been interpreted as the base of the oceanic Monterey microplate (Hoots, 2016) and the dipping geometry of this high velocity anomaly from our model generally agrees with this interpretation. At the conjunction area between the GV and the western SNB, we observe another interesting velocity contrast with low Vs beneath the central GV and west-dipping high Vs beneath the Sierran foothills (Figure 7a and Figure 5b). This feature is generally consistent with the transition of positive to negative velocity gradient (green line in Figure 7a) observed in the Sp receiver function study (Hoots, 2016) as well as the recent P-wave receiver function study (Dougherty et al., 2020).

In addition to the improvement of interface structures, our model also reveals finer Vs structures in the upper mantle compared with the `Jiang2018` model. For example, the well-known high velocity IA has a thickness of ~ 100 km shown in the profiles of AA' and BB' based on the `Jiang2018` model, while the IA in our model has a thickness of about 40 km. The `Jiang2018` model is inverted from frequency-dependent dispersion curves of surface waves which are mostly sensitive to smoothly varying velocities but place very weak constraints on interface structures, making it hard to infer the accurate thickness of the high velocity body in their study. In contrast, TeleFWI used in our joint inversion enables us to image smaller-scale heterogeneities (40 km as shown in Figure 6) and sharp velocity discontinuities, resulting in a more concentrated and thinner high velocity anomaly for IA.

The geometry of the IA provides a piece of key observational evidence in deciphering its origin as either being the foundering lithosphere (e.g., Zandt et al., 2004; Boyd et al., 2004) beneath the southern SNB or representing a fossil slab connected to the Monterey microplate (e.g., Y. Wang et al., 2013; Jiang, Schmandt, Hansen, et al., 2018). In the `Jiang2018` model, the high velocity anomaly dips continuously eastward from the coast to the depth of 200 km beneath the eastern SNB, and is regarded as direct evidence of the fossil slab mechanism. However in our model, this anomaly is truncated at about 100 km by a westward-dipping low Vs body beneath the SNB, separating the shallow IA1 from the deeper IA2 and IA3 beneath the SNB (Figure 7a). There are also considerable differences in the geometry of this low velocity anomaly between profiles AA' and BB'. Along the BB' profile (Figure 7c), the low Vs is relatively weak and the deeper IA2 seems to be attached to the IA1 to form a continuous eastward dipping high velocity body. Therefore, our new model suggests that the shallow IA1 is more likely to be part of the subducted oceanic slab which dips eastward to the depth of at least 100 km beneath the eastern GV, and possibly has a connection with the deeper high velocity anomalies beneath the SNB. The model also reveals possible velocity gaps in the plausible continuous oceanic slab, suggesting that the subducted slab may break off from the western part. The velocity gap may be a localized small-scale feature, which is below the resolution outside the dense CCSE line. To completely constrain the full picture of the 3D geometry of the IA, future deployments of denser stations with more data sets in the off-line region may be needed.

4.3 Limitations and future perspectives

In this study, we have demonstrated the advantage of the joint inversion over individual inversions of surface waves and teleseismic P waves through a series of 3D synthetic tests and an application to seismic data recorded in central California. More specifically, TeleFWI has high resolution in the vicinity of the dense array and can reveal small-scale heterogeneities and constrain sharp velocity boundaries (such as the Moho and LAB) in the upper mantle, while ANAT using broadly distributed stations has relatively uniform ray coverage with a good lateral resolution for Vs structures in the crust and uppermost mantle. The joint inversion enables the construction of a more unified model by combining the sensitivities of surface wave and body wave data.

However, several limitations of the joint inversion may be considered for improvement in future studies. First, the FK-SEM hybrid method adopted in TeleFWI is based on a plane wave assumption which does not consider the spherical curvature of the Earth. To overcome this limitation, the external 1D solver outside the target area in hybrid methods needs to be replaced by 1D efficient global solvers for a spherical Earth model, such as those based on normal modes (Capdeville et al., 2003), direct solution method (DSM, e.g., Monteiller et al., 2013, 2015), and axisymmetric SEM (AxiSEM, e.g., Beller, Monteiller, Operto, et al., 2018). Nevertheless, it is worth noting that the forward simulation of the FK-SEM hybrid method is much faster than the other global hybrid methods mentioned above, and it is sufficiently accurate for modeling teleseismic wavefields when the array aperture is much smaller than epicenter distances (Monteiller et al., 2020). Second, the final Vs model from the joint inversion method represents the average structure constrained by two data sets, and it might not be reliable in certain regions where the inverted structure from different methods deviates from each other significantly. Since TeleFWI suffers from off-line spatial aliasing effects due to insufficient station density and limited data waveform, it would be beneficial to further improve the inversion result at deep depths ($>$ 100 km) by adding more data sets sampling the off-line areas. One significant advantage of adjoint tomography is that the model can continue to be updated whenever new data sets become available. Compared with the relatively scarce high-quality waveforms of scattered waves, there are a large number of traveltime data for other primary seismic phases such as direct P/S, PKP/SKS, etc. Traveltime adjoint tomography of other primary phases could also be included in future joint inversions to further improve the resolution of the Vp and Vs images of the lithospheric mantle.

5 Conclusion

In this study, we propose a joint inversion scheme that fits ambient noise surface waves and teleseismic P waves simultaneously based on 3D seismic wave simulations. The method is applied to ambient noise empirical Green's functions from 60 virtual sources, direct P and scattered waves from 11 teleseismic events in the central California plate boundary region. By comparing the tomographic results from ambient noise adjoint tomography, teleseismic full-waveform inversion and the joint inversion using both field data sets and synthetics from 3D checkerboard models, we demonstrate that the joint inversion outperforms separate inversions as it combines the complementary sensitivities of both towards a more unified model. The final Vs model from our joint inversion delineates a distinct interface between the GV and western SNB in the crust and the LAB underneath the western coast, which are in good agreement with recent receiver function studies. Furthermore, the new model also reveals a refined geometry of the high velocity Isabella Anomaly with a thickness of about 40 km. The shallow Isabella Anomaly is part of the subducted oceanic slab which dips eastward to at least 100 km depth beneath the eastern GV and possibly breaks off at greater depths. This proposed joint inversion scheme can be applied to other regions with both a dense linear array and regional array networks to obtain high-resolution lithospheric images. Additional phases and wavefields can be further incorporated using a similar inversion framework.

Acknowledgments

The seismic data used in this study are downloaded from the Caltech/USGS Southern California Seismic Network (`https://doi.org/10.7914/SN/CI`) and IRIS DMC (`https://ds.iris.edu/ds/nodes/dmc/`). Computations for this study were performed on hardware acquired through the combined funding of Canada Foundation for Innovation (CFI), Ontario Research Fund (ORF), and University of Toronto Startup Fund and partly hosted by the SciNet HPC Consortium. K.Wang and Y. Yang are supported by the Australian Research Council Discovery Grants DP190102940. K. Wang and Q. Liu are supported by the NSERC Discovery Grant 487237. Numerical simulations are performed using the open-source software SPECFEM3D (`https://github.com/geodynamics/specfem3d`). The inversion workflow used in this study is available from `https://github.com/wangkaim8/SPECFEM3D_ANAT`. This is contribution ???? from the ARC Centre of Excellence for Core to Crust Fluid Systems) and ???? in the GEMOC Key Centre.

References

Aki, K., Christoffersson, A., & Husebye, E. S. (1976). Three-dimensional seismic structure of the lithosphere under Montana LASA. *Bulletin of the Seismological Society of America*, *66*(2), 501–524.

Beller, S., Monteiller, V., Combe, L., Operto, S., & Nolet, G. (2018). On the sensitivity of teleseismic full-waveform inversion to earth parametrization, initial model and acquisition design. *Geophysical Journal International*, *212*(2), 1344–1368.

Beller, S., Monteiller, V., Operto, S., Nolet, G., Paul, A., & Zhao, L. (2018). Lithospheric architecture of the South-Western Alps revealed by multiparameter teleseismic full-waveform inversion. *Geophysical Journal International*, *212*(2), 1369–1388.

Bensen, G., Ritzwoller, M., Barmin, M., Levshin, A. L., Lin, F., Moschetti, M., … Yang, Y. (2007). Processing seismic ambient noise data to obtain reliable broad-band surface wave dispersion measurements. *Geophysical Journal International*, *169*(3), 1239–1260.

Bernardino, M. V., Jones, C. H., Levandowski, W., Bastow, I., Owens, T. J., & Gilbert, H. (2019). A multicomponent Isabella anomaly: Resolving the physical state of the Sierra Nevada upper mantle from Vp/Vs anisotropy tomography. *Geosphere*, *15*(6), 2018–2042.

Bostock, M. (2004). Green's functions, source signatures, and the normalization of teleseismic wave fields. *Journal of Geophysical Research: Solid Earth*, *109*(B3).

Boyd, O. S., Jones, C. H., & Sheehan, A. F. (2004). Foundering lithosphere imaged beneath the southern Sierra Nevada, California, USA. *Science*, *305*(5684), 660–662.

Bozdağ, E., Peter, D., Lefebvre, M., Komatitsch, D., Tromp, J., Hill, J., … Pugmire, D. (2016). Global adjoint tomography: first-generation model. *Geophysical Journal International*, *207*(3), 1739–1766.

Capdeville, Y., Chaljub, E., Vilotte, J. P., & Montagner, J. P. (2003). Coupling the spectral element method with a modal solution for elastic wave propagation in global earth models. *Geophysical Journal International*, *152*(1), 34–67. doi: 10.1046/j.1365-246X.2003.01808.x

Chen, M., Huang, H., Yao, H., Hilst, R., & Niu, F. (2014). Low wave speed zones in the crust beneath SE Tibet revealed by ambient noise adjoint tomography. *Geophysical Research Letters*, *41*(2), 334–340.

Chen, M., Niu, F., Liu, Q., Tromp, J., & Zheng, X. (2015). Multiparameter adjoint tomography of the crust and upper mantle beneath East Asia: 1. Model construction and comparisons. *Journal of Geophysical Research: Solid Earth*, *120*(3), 1762–1786.

Dougherty, S. L., Jiang, C., Clayton, R. W., Schmandt, B., & Hansen, S. M. (2020). Seismic evidence for a fossil slab origin for the isabella anomaly. *Geophysical Journal International*, *224*(2), 1188–1196.

Ekström, G., Tromp, J., & Larson, E. W. (1997). Measurements and global models of surface wave propagation. *Journal of Geophysical Research: Solid Earth*, *102*(B4), 8137–8157.

Fang, H., Zhang, H., Yao, H., Allam, A., Zigone, D., Ben-Zion, Y., … van der Hilst, R. D. (2016). A new algorithm for three-dimensional joint inversion of body wave and surface wave data and its application to the Southern California plate boundary region. *Journal of Geophysical Research: Solid Earth*, *121*(5), 3557–3569.

Fichtner, A., Kennett, B. L., Igel, H., & Bunge, H.-P. (2009). Full seismic waveform tomography for upper-mantle structure in the Australasian region using adjoint methods. *Geophysical Journal International*, *179*(3), 1703–1725.

Friederich, W. (2003). The S-velocity structure of the East Asian mantle from inversion of shear and surface waveforms. *Geophysical Journal International*, *153*(1), 88–102.

Gao, H., & Shen, Y. (2014). Upper mantle structure of the Cascades from full-wave ambient noise tomography: Evidence for 3D mantle upwelling in the back-arc. *Earth and Planetary Science Letters*, *390*, 222–233.

Guo, Z., Wang, K., Yang, Y., Tang, Y., John Chen, Y., & Hung, S.-H. (2018). The origin and mantle dynamics of quaternary intraplate volcanism in Northeast China from joint inversion of surface wave and body wave. *Journal of Geophysical Research: Solid Earth*, *123*(3), 2410–2425.

Halldor, B., & Venegas, S. A. (1997). A manual for EOF and SVD analyses of climate data. *McGill University, CCGCR Report*, *97-1*, 52.

Hoots, C. (2016). *Seismic imaging of the lithosphere-asthenosphere boundary with a dense broadband array in central California* (Unpublished master's thesis). University of New Mexico.

Hung, S.-H., Shen, Y., & Chiao, L.-Y. (2004). Imaging seismic velocity structure beneath the Iceland hot spot: A finite frequency approach. *Journal of Geophysical Research: Solid Earth*, *109*(B8).

Jiang, C., & Denolle, M. A. (2020). NoisePy: A new high-performance python tool for ambient-noise seismology. *Seismological Research Letters*, *91*(3), 1853–1866.

Jiang, C., Schmandt, B., Hansen, S. M., Dougherty, S. L., Clayton, R. W., Farrell, J., & Lin, F.-C. (2018). Rayleigh and S wave tomography constraints on subduction termination and lithospheric foundering in central California. *Earth and Planetary Science Letters*, *488*, 14–26.

Jiang, C., Schmandt, B., Ward, K. M., Lin, F.-C., & Worthington, L. L. (2018). Upper mantle seismic structure of Alaska from Rayleigh and S wave tomography. *Geophysical Research Letters*, *45*(19), 10–350.

Jones, C. H., Kanamori, H., & Roecker, S. W. (1994). Missing roots and mantle "drips": Regional Pn and teleseismic arrival times in the southern Sierra Nevada and vicinity, California. *Journal of Geophysical Research: Solid Earth*, *99*(B3), 4567–4601.

Jones, C. H., Reeg, H., Zandt, G., Gilbert, H., Owens, T. J., & Stachnik, J. (2014). P-wave tomography of potential convective downwellings and their source regions, Sierra Nevada, California. *Geosphere*, *10*(3), 505–533.

Kennett, B. L., Engdahl, E., & Buland, R. (1995). Constraints on seismic velocities in the Earth from traveltimes. *Geophysical Journal International*, *122*(1), 108–124.

Kikuchi, M., & Kanamori, H. (1982). Inversion of complex body waves. *Bulletin of the Seismological Society of America*, *72*(2), 491–506.

Komatitsch, D., & Vilotte, J.-P. (1998). The spectral element method: An efficient tool to simulate the seismic response of 2D and 3D geological structures. *Bulletin of the seismological society of America*, *88*(2), 368–392.

Krischer, L., Fichtner, A., Boehm, C., & Igel, H. (2018). Automated large-scale full seismic waveform inversion for North America and the North Atlantic. *Journal of Geophysical Research: Solid Earth*, *123*(7), 5902–5928.

Lay, T., Kanamori, H., Ammon, C. J., Hutko, A. R., Furlong, K., & Rivera, L. (2009). The 2006–2007 Kuril Islands great earthquake sequence. *Journal of Geophysical Research: Solid Earth*, *114*(B11).

Lin, C., Monteiller, V., Wang, K., Liu, T., Tong, P., & Liu, Q. (2019). High-frequency seismic wave modelling of the deep Earth based on hybrid methods and spectral-element simulations: a conceptual study. *Geophysical Journal International*, *219*(3), 1948–1969.

Lin, F.-C., Ritzwoller, M. H., Townend, J., Bannister, S., & Savage, M. K. (2007). Ambient noise Rayleigh wave tomography of New Zealand. *Geophysical Journal International*, *170*(2), 649–666.

Liu, Q., & Gu, Y. (2012). Seismic imaging: From classical to adjoint tomography. *Tectonophysics*, *566*, 31–66.

Liu, Q., & Tromp, J. (2006). Finite-frequency kernels based on adjoint methods. *Bulletin of the Seismological Society of America*, *96*(6), 2383–2397.

Lloyd, A., Wiens, D., Zhu, H., Tromp, J., Nyblade, A., Aster, R., … others (2020). Seismic Structure of the Antarctic Upper Mantle Imaged with Adjoint Tomography. *Journal of Geophysical Research: Solid Earth*, *125*(3).

Lou, X., Van Der Lee, S., & Lloyd, S. (2013). AIMBAT: A python/matplotlib tool for measuring teleseismic arrival times. *Seismological Research Letters*, *84*(1), 85–93.

Lu, Y., Stehly, L., Brossier, R., Paul, A., & Group, A. W. (2020). Imaging Alpine crust using ambient noise wave-equation tomography. *Geophysical Journal International*, *222*(1), 69–85.

Masson, Y., & Romanowicz, B. (2016). Fast computation of synthetic seismograms within a medium containing remote localized perturbations: a numerical solution to the scattering problem. *Geophysical Journal International*, *208*(2), 674–692.

Monteiller, V., Beller, S., Plazolles, B., & Chevrot, S. (2020). On the validity of the planar wave approximation to compute synthetic seismograms of teleseismic body waves in a 3-D regional model. *Geophysical Journal International*.

Monteiller, V., Chevrot, S., Komatitsch, D., & Fuji, N. (2013). A hybrid method to compute short-period synthetic seismograms of teleseismic body waves in a 3-D regional model. *Geophysical Journal International*, *192*(1), 230–247.

Monteiller, V., Chevrot, S., Komatitsch, D., & Wang, Y. (2015). Three-dimensional full waveform inversion of short-period teleseismic wavefields based upon the SEM-DSM hybrid method. *Geophysical Journal International*, *202*(2), 811–827. doi: 10.1093/gji/ggv189

Montelli, R., Nolet, G., Dahlen, F., Masters, G., Engdahl, E. R., & Hung, S.-H. (2004). Finite-frequency tomography reveals a variety of plumes in the mantle. *Science*, *303*(5656), 338–343.

Moschetti, M., Ritzwoller, M., Lin, F.-C., & Yang, Y. (2010). Crustal shear wave velocity structure of the western United States inferred from ambient seismic noise and earthquake data. *Journal of Geophysical Research: Solid Earth*, *115*(B10).

Nocedal, J., & Wright, S. (2006). *Numerical optimization*. Springer Science & Business Media.

Nunn, C., Roecker, S. W., Priestley, K. F., Liang, X., & Gilligan, A. (2014). Joint inversion of surface waves and teleseismic body waves across the Tibetan collision zone: the fate of subducted Indian lithosphere. *Geophysical Journal International*, *198*(3), 1526–1542.

Obrebski, M., Allen, R. M., Pollitz, F., & Hung, S.-H. (2011). Lithosphere–asthenosphere interaction beneath the western United States from the joint inversion of body-wave traveltimes and surface-wave phase velocities. *Geophysical Journal International*, *185*(2), 1003–1021.

Peter, D., Komatitsch, D., Luo, Y., Martin, R., Le Goff, N., Casarotti, E., … Others (2011). Forward and adjoint simulations of seismic wave propagation on fully unstructured hexahedral meshes. *Geophysical Journal International*, *186*(2), 721–739.

Pienkowska, M., Monteiller, V., & Nissen-Meyer, T. (2020). High-frequency global wavefields for local 3D structures by wavefield injection and extrapolation. *Geophysical Journal International*. doi: 10.1093/gji/ggaa563

Plessix, R.-E. (2006). A review of the adjoint-state method for computing the gradient of a functional with geophysical applications. *Geophysical Journal International*, *167*(2), 495–503.

Pratt, R. G. (1999). Seismic waveform inversion in the frequency domain; Part 1, Theory and verification in a physical scale model. *Geophysics*, *64*(3), 888–901.

Raikes, S. A. (1980). Regional variations in upper mantle structure beneath southern California. *Geophysical Journal International*, *63*(1), 187–216.

Ritzwoller, M. H., Shapiro, N. M., Barmin, M. P., & Levshin, A. L. (2002). Global surface wave diffraction tomography. *Journal of Geophysical Research: Solid Earth*, *107*(B12), ESE–4.

Sager, K., Boehm, C., Ermert, L., Krischer, L., & Fichtner, A. (2020). Global-Scale Full-Waveform Ambient Noise Inversion. *Journal of Geophysical Research: Solid Earth*, *125*(4), e2019JB018644.

Saygin, E., & Kennett, B. L. (2010). Ambient seismic noise tomography of Australian continent. *Tectonophysics*, *481*(1-4), 116–125.

Schmandt, B., & Humphreys, E. (2010). Complex subduction and small-scale convection revealed by body-wave tomography of the western United States upper mantle. *Earth and Planetary Science Letters*, *297*(3-4), 435–445.

Shapiro, N. M., Campillo, M., Stehly, L., & Ritzwoller, M. H. (2005). High-resolution surface-wave tomography from ambient seismic noise. *Science*, *307*(5715), 1615–1618.

Shen, W., Ritzwoller, M. H., & Schulte-Pelkum, V. (2013). A 3-D model of the crust and uppermost mantle beneath the Central and Western US by joint inversion of receiver functions and surface wave dispersion. *Journal of Geophysical Research: Solid Earth*, *118*(1), 262–276.

Sigloch, K., McQuarrie, N., & Nolet, G. (2008). Two-stage subduction history under North America inferred from multiple-frequency tomography. *Nature Geoscience*, *1*(7), 458.

Sun, M., Zhang, J., & Zhang, W. (2017). Alternating first-arrival traveltime tomography and waveform inversion for near-surface imaging. *Geophysics*, *82*(4), R245–R257.

Tao, K., Grand, S. P., & Niu, F. (2018). Seismic structure of the upper mantle beneath eastern Asia from full waveform seismic tomography. *Geochemistry, Geophysics, Geosystems*, *19*(8), 2732–2763.

Tape, C., Liu, Q., Maggi, A., & Tromp, J. (2009). Adjoint tomography of the southern California crust. *Science*, *325*(5943), 988–992.

Tape, C. H. (2009). *Seismic tomography of southern California using adjoint methods* (Unpublished doctoral dissertation). California Institute of Technology.

Tong, P., Chen, C.-w., Komatitsch, D., Basini, P., & Liu, Q. (2014). High-resolution seismic array imaging based on an SEM-FK hybrid method. *Geophysical Journal International*, *197*(1), 369–395. doi: 10.1093/gji/ggt508

Tong, P., Komatitsch, D., Tseng, T.-L., Hung, S.-H., Chen, C.-W., Basini, P., & Liu, Q. (2014). A 3-D spectral-element and frequency-wave number hybrid method for high-resolution seismic array imaging. *Geophysical Research Letters*, *41*(20), 7025–7034.

Tromp, J. (2020). Seismic wavefield imaging of Earth's interior across scales. *Nature Reviews Earth & Environment*, 1–14. doi: https://doi.org/10.1038/s43017-019-0003-8

Tromp, J., Tape, C., & Liu, Q. (2005). Seismic tomography, adjoint methods, time reversal and banana-doughnut kernels. *Geophysical Journal International*, *160*(1), 195–216.

van der Hilst, R. D., Widiyantoro, S., & Engdahl, E. (1997). Evidence for deep mantle circulation from global tomography. *Nature*, *386*(6625), 578–584.

Virieux, J., & Operto, S. (2009). An overview of full-waveform inversion in exploration geophysics. *Geophysics*, *74*(6), WCC1–WCC26.

Wang, K., Jiang, C., Yang, Y., Schulte-Pelkum, V., & Liu, Q. (2020). Crustal deformation in southern California constrained by radial anisotropy from ambient noise adjoint tomography. *Geophysical Research Letters*, *47*(12), e2020GL088580.

Wang, K., Liu, Q., & Yang, Y. (2019). Three-Dimensional Sensitivity Kernels for Multicomponent Empirical Green's Functions From Ambient Noise: Methodology and Application to Adjoint Tomography. *Journal of Geophysical Research: Solid Earth*, *124*(6), 5794–5810.

Wang, K., Yang, Y., Basini, P., Tong, P., Tape, C., & Liu, Q. (2018). Refined crustal and uppermost mantle structure of southern California by ambient noise adjoint tomography. *Geophysical Journal International*, *215*(2), 844–863.

Wang, Y., Chevrot, S., Monteiller, V., Komatitsch, D., Mouthereau, F., Manatschal, G., ... others (2016). The deep roots of the western Pyrenees revealed by full waveform inversion of teleseismic P waves. *Geology*, *44*(6), 475–478.

Wang, Y., Forsyth, D. W., Rau, C. J., Carriero, N., Schmandt, B., Gaherty, J. B., & Savage, B. (2013). Fossil slabs attached to unsubducted fragments of the Farallon plate. *Proceedings of the National Academy of Sciences*, *110*(14), 5342–5346.

West, M., Gao, W., & Grand, S. (2004). A simple approach to the joint inversion of seismic body and surface waves applied to the southwest US. *Geophysical research letters*, *31*(15).

Woodhouse, J. H., & Dziewonski, A. M. (1984). Mapping the upper mantle: Three-dimensional modeling of Earth structure by inversion of seismic waveforms. *Journal of Geophysical Research: Solid Earth*, *89*(B7), 5953–5986.

Xie, J., Chu, R., & Yang, Y. (2018). 3-D upper-mantle shear velocity model beneath the contiguous united states based on broadband surface wave from ambient seismic noise. *Pure and Applied Geophysics*, *175*(10), 3403–3418.

Yang, Y., Ritzwoller, M. H., Levshin, A. L., & Shapiro, N. M. (2007). Ambient noise Rayleigh wave tomography across Europe. *Geophysical Journal International*, *168*(1), 259–274.

Yang, Y., Ritzwoller, M. H., Lin, F.-C., Moschetti, M., & Shapiro, N. M. (2008). Structure of the crust and uppermost mantle beneath the western United States revealed by ambient noise and earthquake tomography. *Journal of Geophysical Research: Solid Earth*, *113*(B12).

Yao, H., van Der Hilst, R. D., & De Hoop, M. V. (2006). Surface-wave array tomography in SE Tibet from ambient seismic noise and two-station analysis—I. Phase velocity maps. *Geophysical Journal International*, *166*(2), 732–744.

Zandt, G., Gilbert, H., Owens, T. J., Ducea, M., Saleeby, J., & Jones, C. H. (2004). Active foundering of a continental arc root beneath the southern Sierra Nevada in California. *Nature*, *431*(7004), 41–46.

Zhang, C., Yao, H., Liu, Q., Zhang, P., Yuan, Y. O., Feng, J., & Fang, L. (2018). Linear array ambient noise adjoint tomography reveals intense crust-mantle interactions in North China Craton. *Journal of Geophysical Research: Solid Earth*, *123*(1), 368–383.

Zhang, C., Yao, H., Tong, P., Liu, Q., & Lei, T. (2020). Joint inversion of linear array ambient noise surface-wave and teleseismic body-wave data based on an adjoint-state method. *Acta Geophysica Sinica*, *63*(11), 4065–4079.

Zhang, H., Maceira, M., Roux, P., & Thurber, C. (2014). Joint inversion of body-wave arrival times and surface-wave dispersion for three-dimensional seismic structure around SAFOD. *Pure and Applied Geophysics*, *171*(11), 3013–3022.

Zheng, S., Sun, X., Song, X., Yang, Y., & Ritzwoller, M. H. (2008). Surface wave tomography of China from ambient seismic noise correlation. *Geochemistry, Geophysics, Geosystems*, *9*(5).

Zhou, Y., Dahlen, F., & Nolet, G. (2004). Three-dimensional sensitivity kernels for surface wave observables. *Geophysical Journal International*, *158*(1), 142–168.

Zhu, H., Bozdağ, E., Peter, D., & Tromp, J. (2012). Structure of the European upper mantle revealed by adjoint tomography. *Nature Geoscience*, *5*(7), 493–498.

A Teleseismic traveltime estimation for FK-SEM

The traveltime delay from the initial wavefront through (x_0, y_0, z_0) to a surface point at $(x_r, y_r, 0)$ can be calculated as:

$$T_r^{FK} = p[(x_r - x_0)\cos\phi + (y_r - y_0)\sin\phi] + \eta_0 * (z_{bot} - z_0) + \sum_{m=1}^{n} \eta_m * H_m, \qquad \text{(A.1)}$$

where

$$p = \frac{\sin\theta}{v_0};\ \eta_m = \sqrt{\frac{1}{v_m^2} - p^2} \qquad \text{(A.2)}$$

In above, ϕ is the azimuth, H_m is the thickness of the m'th layer. z_{bot} is the z coordinate of the bottom of all layers (top of half space). p is the horizontal slowness (ray parameter) which is conserved along the ray and θ is the incident angle. v_m is the P or S wave velocity in m'th layer and the corresponding vertical slowness is η_m. Note $m = 0$ indicates the velocity/slowness in the halfspace.